Biophysical Journal Volume 102 March 2012 1224–1233

The Influence of a Biologically Relevant Substratum Topography on Human Aortic and Umbilical Vein Endothelial Cells

Clayton T. McKee,[†*] Joshua A. Wood,[†] Irene Ly,[†] Paul Russell,[†] and Christopher J. Murphy[†‡*]
[†]Department of Surgical and Radiological Sciences, School of Veterinary Medicine and [‡]Department of Ophthalmology and Vision Science, School of Medicine, University of California, Davis, California

ABSTRACT A topographically patterned substrate with stochastic surface order that closely mimics the topographic features of native basement membranes has been fabricated to investigate the influence of topographic biophysical cueing on human aortic and umbilical vein endothelial cells. The stochastic substrate was fabricated by first generating a highly porous polyelectrolyte multilayer film of poly(acrylic acid) and poly(allylamine hydrochloride) followed by replicate production of this biomimetic topography via soft lithography. These substrates, which are easy to prepare and replicate, possess a number of prominent features associated with in vivo vascular basement membrane (interwoven ridges and grooves, bumps, and pores), which have typically been studied as singular features that frequently possess anisotropic surface order (e.g., alternating ridges and grooves). When compared to a flat surface of identical chemistry, these biomimetic topographies influenced a number of important cellular behaviors associated with the homeostasis and degradation of vascular tissues. These include modulating cell migration rate and directional persistence, proliferation rate, and gene expression associated with regulation and remodeling of vascular tissues as well as inflammation.

INTRODUCTION

It is well established that the physical attributes of the extracellular environment (e.g., topography and/or compliance) can inform internal cell processes and responses to external stimuli (1–6). The response of cells to these attributes is particularly relevant given the complex milieu of physical cues that cells can interact with in vivo (often termed biophysical cueing). Biophysical cues are not static and can alter with age (7), during disease progression (8) or in response to therapeutic intervention (9), which has motivated the creation of novel biomimetic cell cultureware to obtain a more complete understanding of cell responses to biophysical cues. Biomimetic surfaces, which can be fabricated with natural (collagen (10), matrigel (11), silicon (12)), or synthetic polymers (13), are typically designed to understand a single physical property of the extracellular environment in isolation. For example, soft lithography (14) has been used to generate highly ordered topographic arrays of three of the most commonly observed, and studied, aspects of extracellular matrix: ridges and grooves (12), bumps (15), and pores (16), all with dimensions in the biological range (nm to μm). However, work by Liliensiek et al. (17), and others (18–20) has shown that the basement membrane of many tissues, including vascular tissues (17), display a complex mixture of these topographic features in a stochastic setting. To better understand how the combination of multiple topographic features influence primary human umbilical vein and aortic endothelial cells (HUVECs and HAECs), we have generated highly porous polyelectrolyte multilayer films (PEMs) that closely mimic the stochastic nature of in vivo vascular basement membrane topography. We have done this via a modification of the method first demonstrated by Mendelsohn et al. (21). To ensure that multiple experiments could be conducted with identical surface features, soft lithography was employed to replicate the topographic milieu of these PEMs in cell cultureware. Differences in proliferation and migration rate, directional persistence, and gene expression for both cell types, as well as the inflammatory response for HAECs when cultured on these stochastic, topographically biomimetic surfaces were quantified.

METHODS

Substrate fabrication and nanolithography

Master topographies, for use in soft lithography, were generated by forming PEMs of poly(acrylic acid) (PAA, MW $\cong$ 60,000, Polysciences, Warrington, PA) and poly(allylamine hydrochloride) (PAH, MW $\cong$ 160,000, Alfa Aesar, Ward Hill, MA) on glass microscope slides. Solutions of PAA and PAH were prepared at 0.01 M (based on MW of monomer unit) at a pH of 3.5 and 7.5, respectively. Solutions were prepared using ultrahigh purity water (18.2 MΩ.cm) and the pH was controlled with NaOH and HCl. Before PEM formation, the glass microscope slides were plasma treated (Harrick Plasma Cleaner, Harrick Plasma, Ithaca, NY) for 1 min and then immediately silanated by exposure to 3-aminopropyltrimethoxysilane (APS, Sigma Aldrich, St. Louis, MO) vapor for 1 h under vacuum. After 1 h in the presence of APS vapor, the APS was removed and the samples were left under vacuum for 24 h to remove unreacted APS. These amine-terminated glass slides were initially submerged in PAA for 15 min, followed by two, 1-min submersions in ultrahigh purity water, and then submerged in PAH for 15 min (22). This process was repeated until 10 layers (PAA/PAH = one layer) were generated. At the end of the dipping process, the samples were blown dry with high-purity nitrogen and then dehydrated in an oven at 60°C for 1 h. Samples were then dipped in a solution of HCl at a pH of 2.3 for 1 min, which resulted in a highly porous, phase separated PEM (21). Samples were immediately

Submitted November 28, 2011, and accepted for publication January 31, 2012.

*Correspondence: cjmurphy@ucdavis.edu or clayton.mckee@gmail.com

Editor: Cecile Sykes.

0006-3495/12/03/1224/10 $2.00
doi: 10.1016/j.bpj.2012.01.053

blown dry with high-purity nitrogen and placed in an oven at 60°C for 1 h. If these porous PEMs were reexposed to solution, the porous structure was rapidly lost. To maintain the long-term stability of the porous structure of the PEM, the APS coated slide containing the PEM was placed in an oven at 200°C for 20 min. This cross-links the PAA and PAH, as well as the base PAA layer to the amine-terminated glass slide via amide bond formation. PEMs that were not cross-linked to an APS coated glass slide would typically detach from the surface if left in solution for more than 3 or 4 days (PEMs cross-linked to the APS did not detach). Although detachment is useful in recovering the thin film from the glass, cell culture experiments dictate the PEM to remain attached to the glass.

The following procedure was used to recreate identical replicates of the master porous PEM described previously. The master PEMs were first dipped in a concentrated solution of sodium dodecyl sulfate (SDS, 16 mM) and then blown dry with ultrahigh purity nitrogen. The concentrated SDS solution ensured there was an adequate amount of SDS in the bulk to adsorb to the increased surface area of the porous PEM, and ensured that subsequent polydimethylsiloxane (PDMS) molds of the topography detached, without damaging the PEM on the glass surface. High-fidelity replicates of the nanoporous features of the PEM were created using a composite two-layer PDMS stamp (13), consisting of a thin and hard PDMS layer (*h*PDMS) attached to a thick support of 184 PDMS. The composite stamp was formed as follows: 2 drops of 2,4,6,8-tetramethyl-2,4,6,8-tetravinylcyclotetrasiloxane (396281-10 ML, Sigma Aldrich) and 50 μl of platinum-divinyltetramethyldisiloxane complex in xylene (SIP6831.2-LC, Gelest, Morrisville, PA) were gently mixed with 3.4 grams of 7.0–8.0% (vinylmethylsiloxane)-dimethylsiloxane copolymer, trimethylsiloxy terminated (VDT-731, Gelest). This solution was quickly degassed (1–2 min). One gram of 25–30% (methylhydrosiloxane)-dimethylsiloxane copolymer, trimethylsiloxane terminated (HMS-301, Gelest) was gently mixed with the degassed solution. A dime-sized volume of the polymer solution was poured onto the center of the master porous PEM, which was then spun at 4000 rpm for 40 s. This thin film was cured for 30 min at 60°C to produce the *h*PDMS layer. At the end of 30 min a thick layer of Sylgard 184 PDMS was poured onto the slide and was cured for 3 h at 60°C. Once the PDMS was cured, the composite mold was peeled from the master PEM. Subsequent replicates of the PEM were generated by molding NOA81 to the composite PDMS stamp, by first spin coating NOA81 to a plasma cleaned microscope slide at 4000 rpm for 40 s and then pressing the PDMS stamp into the thin film. This was subsequently ultraviolet (UV)-cured for 40 min. See Fig. 2 *A* for an atomic force microscopy (AFM) height image of the NOA81 replicate of the porous PEM, which will be referred to as synthetic membranes. Finally, flat surfaces of NOA81 were generated via spin coating and UV-curing so that the cellular behaviors on the synthetic membranes could be compared to flat surfaces of identical chemistry. NOA81 is a proprietary mercapto-ester compound of Norland Products (Cranbury, NJ), which is supplied as a single component liquid adhesive that will cure in seconds to a rigid polymer when exposed to UV light. In this regard, the stiffness of cured NOA81 is similar to tissue-culture polystyrene. Our research group has previously demonstrated NOA81 as a suitable material for cell culture (3,5).

Cell culture

HUVECs and HAECs were maintained in endothelial basal media supplemented with EGM-2 BulletKit (Lonza, Walkerville, MD). The BulletKit contains GA-1000, hEGF, fetal bovine serum, heparin, ascorbic acid, R3-IGF, VEGF, hFGF-B, and hydrocortisone. During culture and migration assays, cells were maintained at 37°C and 5% CO_2.

Cell migration analysis via a custom automated cell tracker

Time-lapse observations of cells were obtained on both the flat and membrane surfaces over a 12-h time period, with a collection rate of one frame every 8 min (90 frames). Cells were imaged in phase contrast using an inverted light microscope (Zeiss, Axio Observer A1, Carl Zeiss, Thornwood, NY) with a 10× objective. Cells from a minimum of 10 separate locations were imaged for each condition. Cells were plated at 75,000 cells per plate, which ensured a cell population that was sparse enough for single cell tracking. Cell inclusion for analysis was limited to those cells that remained within the frame during the entire 12-h timelapse and to those that did not undergo division. This resulted in cell counts of 30–50 cells for each condition.

Manual cell tracking (visual location and recording of the cell X and Y pixel data) is a very time consuming and subjective process. We have therefore written an algorithm that automatically tracks and records the location of a cell, as its position changes during the course of the time-lapse movie. The source code for this algorithm was written with the programming and statistical analysis software package IgorPro (Wavemetics, Lake Oswego, OR). The programming language of IgorPro is very similar to C. A detailed description of the algorithm is supplied in the Supporting Material. The migration path of all cells in this work were collected by tracking the darkest region of the cell, which in phase contrast microscopy at 10× magnification, is predominantly the central region of the cell. We used the manual tracking feature available in AxioVision 4.6 (Carl Zeiss, Germany) as a controlled test to compare the output of our algorithm. Our automated tracker, including the source code for the algorithm, is available from the first author but is specific to IgorPro.

Cell proliferation

Five-day proliferation assays were conducted to measure the proliferation rate of the endothelial cells and were performed in triplicate. Cells were plated at 100,000/plate on day 1 and then imaged the following day to determine the initial cell count. The cell count of the slide was determined by collecting five images along the length of the slide, determining the average number of cells/image and then using this to determine the approximate number of cells per plate. Cells were then left in an incubator at 37°C and 5% CO_2 until day five. On day five, the plates were reimaged and the approximate number of cells per plate was again determined. The proliferation rate was quantified by determining the ratio of the number of cells on day 5 to the number of cells on day 2. To compare the difference between cells cultured on the flat surfaces to cells cultured on the synthetic membrane, we normalized the results to the proliferation rate measured on flats (i.e., normalized proliferation rate of one for flats).

Cell directional persistence

Cells in motion tend to maintain their direction of motion for small periods of time (23). This is known as directional persistence. To determine the influence of the synthetic membrane on directional persistence of the cells, we generated histograms of the turning angle observed between three separate positions in the migration path of a cell, as a function of increasing time interval between observation positions. This is demonstrated graphically in Fig. 1. From compiled values of measured turning angles, we generated histograms of the frequency of 0°–10° turns (persistent motion) and 170°–180° turns (antipersistent) as a function of an increasing observation time interval. For small time intervals, a histogram of turning angles should show an increased number of persistent turns as compared to antipersistent. As the time interval increases, the frequency of persistent turns decrease and the antipersistent turns increase. For example, at large enough time intervals, if the cell migration path is random, histograms of persistent and antipersistent turns would be evenly distributed between 0° and 180° and would coincide with one another. We define the time interval of persistent motion, by visually noting the point in which the frequency of persistent turns becomes constant with the increasing time interval. We have additionally quantified the influence of the substrate on the time frame of directional persistence by determining the decay length, δ (min), of exponential fits to the frequency of persistent motion (FPM) versus observation

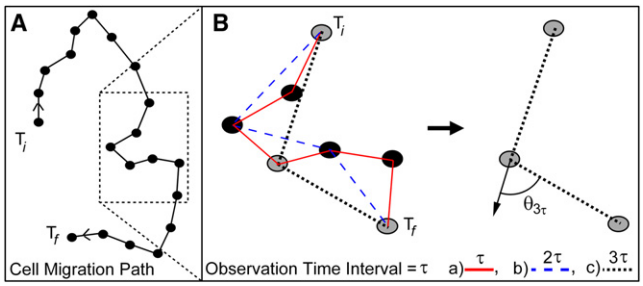

FIGURE 1 (*A*) Hypothetical cell migration path from an initial time point, T_i, to a final time point T_f. (*B*) Demonstration of how the cell turning angle is measured as a function of the cell path, as well as for increasing time interval, τ. Three different observational time intervals are shown (*a-solid red*, *b-dashed blue*, and *c-dotted black lines*). The turning angle θ is defined by the angle formed between a forward progression of the intermediate time point and the final time point (shown for an observation time interval of 3τ). The shorter the time interval the larger the number of measured turning angles. For example, the number of measured turning angles in the subset path in *B* would be five for τ, three for 2τ, and one for 3τ. With an increasing time interval, the measured cell turning angle is increasingly distributed in a random fashion between 0° and 180°.

time interval (T) (FPM $\approx \exp(-T/\delta)$). The larger the decay length the longer the time frame of directional persistence.

Gene expression

Both HUVECs and HAECs were plated at 100,000 cells per plate and allowed to culture for 3 days on the flat and membrane surfaces before RNA extraction. Expression of SPARC (secreted protein acidic and rich in cysteine), PECAM (platelet endothelial cell adhesion molecule), and MMP-2 (matrix metalloproteinase-2) was quantified for both HUVECs and HAECs. The influence of TNF-α (tumor necrosis factor-alpha) on the expression of ICAM-1 (intercellular adhesion molecule-1) in HAECs was also studied. For these experiments, HAECs were exposed to 10 ng/ml TNF-α for 12 h before RNA extraction. We did not study TNF-α with HUVECs as cells derived from umbilical veins are not classically known to be exposed to inflammatory cytokines in the context of cardiovascular disease. RNA was extracted using the Qiagen Rneasy kit according to the manufacturer's protocol (Qiagen, Valencia, CA). Semiquantitative real-time polymerase chain reaction was performed using 75 ng of RNA per reaction and a one-step TaqMan kit with commercially available aptamers for SPARC, PECAM, MMP-2, and ICAM-1 (Hs00277762_M1, Hs00169777_m1, Hs0024442_m1, and Hs00164923_m1, respectively, Applied Biosystems, San Mateo, CA). Reverse transcription occurred for 30 min at 50°C followed by 95°C for 10 min. Amplification of the cDNA occurred for 40 cycles at 60°C for 1 min, followed by 95°C for 15 s. Glyceraldehyde 3-phosphate dehydrogenase, Hs99999905_m1 (Applied Biosystems) served as our internal control gene. At least three reactions were run for each sample and the experiment was performed in triplicate. Gene expression was normalized to the expression of mRNA from cells on flat surfaces.

AFM

The topographic features of the porous surface were quantified from the piezo height response of a contact mode image obtained with an atomic force microscope (MFP-3D-BIO, Asylum Research, Santa Barbara, CA). The surfaces were scanned using silicon nitride cantilevers, which have a square pyramid tip incorporated at the free end ($k = 0.06$N/m, PNP-TR-50, Nano And More, Lady's Island, SC). To ensure an undistorted view of the actual sample, Asylum's Argyle Light software was used to match the *Z*-scale of the topographic features (their height) to the lateral *X* and *Y* dimension of the image (i.e., a 1:1 aspect ratio).

Statistical analysis

Statistical significance and *p*-values for the migration and proliferation assays were determined by *t*-test analysis (mean ± standard deviation). Statistical significance and *p*-values for gene expression results were determined using Sigma Plot 11 (Systat Software, Chicago, IL) with the following tests: For HUVECs and HAECs, Mann-Whitney exact rank sum tests were used to determine significance between substrates. For HAECs, Kruskal-Wallis exact one-way analysis of variance on ranks tests was used to determine significance among groups. Significance was set at $p < 0.05$ for all analyses (mean ± standard error of the mean).

RESULTS

During the formation step of the porous PEM, we found that the initially transparent PEM-coated slide became slightly cloudy after exposure to the acidic solution and that the opacity was proportional to the thickness of the film. For this reason we limited our PEMs to 10 layers. The opacity of the porous PEM was also replicated onto the NOA81 membrane surface (NOA81 flat surfaces cured as a fully transparent solid), indicating the cloudiness was due primarily to light scattering from the outermost face of the topography and not precipitate formation within the PEM film. In solution, the opacity was almost undetectable and Fig. S1 shows that it had no apparent effect on the clarity of phase contrast images of the cells on the synthetic membrane. We chose not to use the PEM surfaces directly for cell culture, because we found that the porous structure was exquisitely sensitive to slight differences in the pH of the dipping condition and was therefore difficult to obtain exact replicates between experiments. (We also found that the pH of the dipping solution would increase with each PEM-coated slide that we dipped, as hydrogen ions were depleted from solution. To avoid this problem we started with a large volume of HCl solution from which we removed aliquots for each dipped PEM.) The NOA81 replicates however, could be mass-produced with identical features from a single master PEM that best represented native basement membrane. This was particularly helpful considering the number of experiments that needed to be conducted as well as the ability to directly compare differences between cell types. Fig. 2 *A* is a 20 μm^2 AFM height image of the NOA81 replicate of the porous polyelectrolyte multilayer. This topography was conserved over multiple imaged positions on the replicate. Fig. 2 *B* is a scanning electron microscopy image of inferior vena cava basement membrane from a Rhesus macaque (17) (pore size 49 ± 2 nm, ridge diameter 24 ± 0.6 nm) . The article, which the inset image came from, also contains a number of other vascular basement membranes with similar features. The synthetic membrane in Fig. 2 was composed of pores, ranging from ~200 nm up to ~1.5 μm, with the majority

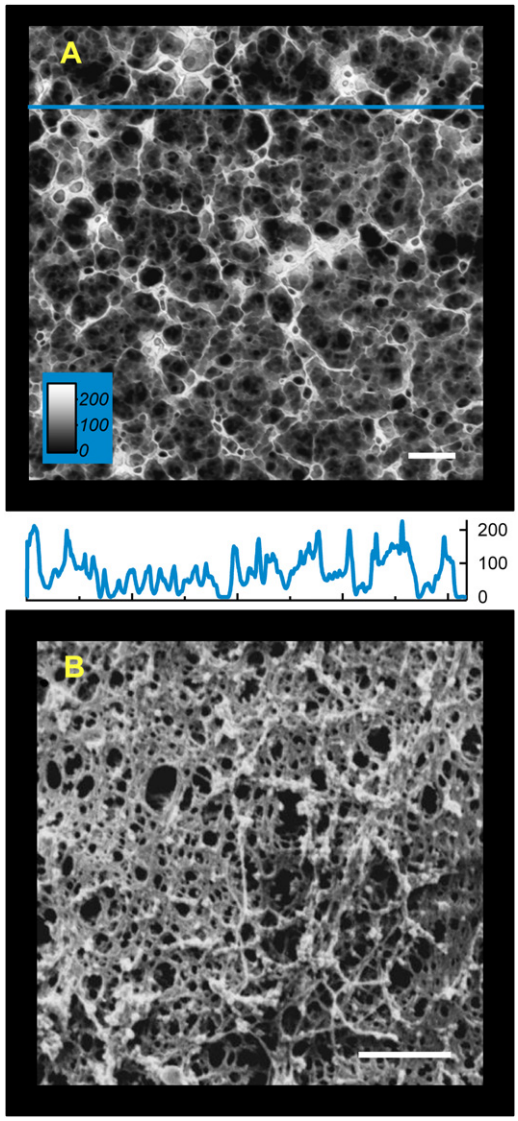

FIGURE 2 (*A*) AFM height mode image of the NOA81 replicate of the porous PEM (scale bar 2 μm). A cross section (*blue line*) is shown, to better show the height of the features (the scale is in nanometers). (*B*) Scanning electron microscope image of inferior vena cava basement membrane from a Rhesus macaque (scale 600 nm) (17). Reprinted with permission from Tissue Engineering A, Mary Anne Liebert, Publishers.

of pores being submicroscopic (pore depth ranged from ~50 to 300 nm). The root mean-square roughness of the sample was 61.6 nm and the difference in surface area (compared to a flat surface) was 10.6%. A cross section of the synthetic membrane is demonstrated between the images. The surface was also composed of ridges and bumps that were interconnected with the porous network, meeting our criteria for a biomimetic topography that was composed of the three major topographic components of in vivo basement membrane. We consider the topographic substrate we have created as an approximate representation, which importantly encapsulates the sum of the stochastic topographic features found in vivo. If we approximate a cell occupying 50 square microns and assume all pores at 500 nm^2, the cell would then be simultaneously interacting with 1×10^5 individual pores on the substrate.

Movie S1 shows the ability of our automated tracker to follow the position of a moving cell over the data collection time interval. We tracked the darkest location within the cell for all cell tracks. With a 10× objective, proper Köhler illumination and tracking parameters, the algorithm-chosen tracked position was centrally located within the cell; this position was often observed to be nucleoli within the nucleus. The automated tracker successfully tracked upward of 80% of the cells that met our inclusion criteria for a given movie, negating the need for manual tracking. Given the *X* and *Y* pixel coordinates of the moving cell and the scale of the image (micrometers/pixel), it was easy to simultaneously output the distance moved and migration rate. Movie S1 also compares the position chosen by our algorithm and a manually tracked location. The efficiency of our tracker was quantified by comparing the time required to automatically or manually track (AxioVision) the location of the 40 HUVEC cells used in our analysis. Our automated tracker typically tracked a cell in <10 s and required ~30 min to track and output the results (migration, proliferation, and persistence) for all the included cells within the 10 positions collected for analysis. Manually tracking the same cells using the AxioVision software took three times longer than automated tracking (including analysis of migration rate). The influence of the substratum topography on the trend in migration rate of HUVEC cells on the synthetic membrane and flats were consistent between our automated tracker and AxioVision's manual tracker (data not shown).

Both HUVECs and HAECs (as well as corneal epithelial and human trabecular meshwork cells, data not shown) adhere, spread, migrate, and proliferate on these topographic substrates, without the need for additional chemical coatings, such as fibronectin or collagen, to assist in cell adhesion. Cells in culture remained viable through confluence, indicating no deleterious effects from the topography or leaching of chemicals from the UV-cured NOA81. The migration and proliferation rate of these cells on the synthetic membrane and flat surfaces are demonstrated in Fig. 3. Both HUVECs and HAECs had similar migration rates on the synthetic membrane surfaces, with values of 1.04 ± 0.16 and 1.02 ± 0.19 μm/min, respectively (Fig. 3, *top*). The absence of the substratum topography on migration rate was however, more pronounced for HAECs. The effect of the synthetic membrane was to increase the rate of both cell types (on flats, HUVECs - 0.91 ± 0.21 and HAECs - 0.70 ± 0.20 μm/min). The trend between the migration rate for HUVEC cells on the synthetic membrane and flats was consistent when manually tracked with AxioVision 3.6. However, when manually tracked, the absolute magnitudes in migration rates were slightly decreased for both substrate conditions

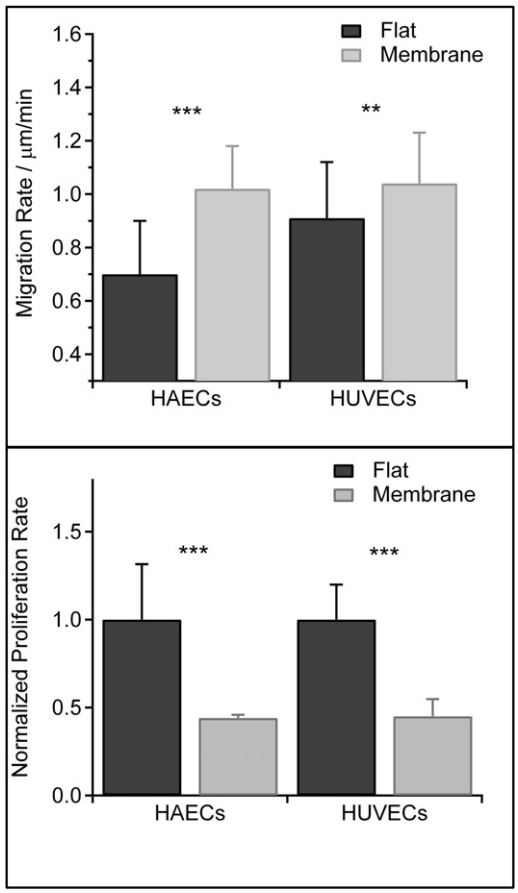

FIGURE 3 Migration rate of both HUVECs and HAECs was significantly increased when cultured on the synthetic membrane as compared to the flat surfaces. Proliferation rates were significantly decreased for both cell types, when cultured on the synthetic membrane (*** $\equiv p < 0.001$, ** $\equiv p = 0.01$).

(1.03 $\pm$ 0.12 and 0.84 $\pm$ 0.22 μm/min, membrane, and flat, respectively). The proliferation rate was significantly reduced for both cell types with normalized proliferation rates that were approximately half the rate for cells cultured on flat surfaces (Fig. 3 *B*). Nonnormalized results showed that HUVECs proliferated ~1.4 times faster than HAECs.

Fig. 4 shows how the synthetic membrane influences the directional persistence of migrating cells for both substrate conditions. As the observation time interval increased, the frequency of measured persistent turns (0°–10° turns) decreased as expected. Both cell types demonstrated a reduced directional persistence time on the synthetic membrane compared to flats. The time interval of directional persistence was ~30 min for both HAECs and HUVECs on the synthetic membrane and ~60 min on the flat surfaces. Exponential fits to the data presented in Fig. 4 also show an increased decay length, δ, for cells cultured on flat surfaces, which is consistent with the observed increase in directional persistence time. The loss of directional persistence over these time frames was also correlated with an increase in antipersistent migration (170°–180°). With increasing time interval, beyond the time frame of persistent motion, both cell types on the flat surfaces had an increased probability of returning on the same path they just migrated upon. This is demonstrated by an increasing percentage of antipersistent turns over persistent turns after the time interval of directional persistence. Both cell types did not preferentially migrate either forward or backward along their migration path on the membrane surface after the loss in directional persistence, as noted by the similarity in the percentage of persistent and antipersistent turns with an increasing time interval.

The influence of the topographic membrane on gene expression was dependent on cell type, as shown in Figs. 5 and 6. The bar graphs show the relative gene expression as a function of substrate type. The *p*-values for significance in Fig. 5 are included in the caption. Below the bar graphs in Fig. 6 there are tables that show the *p*-values when various conditions are compared. For example, there was a significant decrease ($p = 0.048$) in the expression of ICAM-1 when HAECs cultured on the synthetic membrane were exposed to 10 ng/ml TNF-α for 12 h (SM w/TNF) as compared to the flat surface with TNF-α (Flat w/TNF). The combined influence of the topography and TNF-α had a marked effect on the expression MMP-2, SPARC, and PECAM in HAECs as well, with all being significantly downregulated on the synthetic membrane as compared to flats. With the exception of ICAM-1, cells cultured on flat surfaces had no significant response to TNF-α. Although the trends in gene expression of MMP-2 and SPARC were similar for both HUVECs and HAECs, only HUVECs had a significantly downregulated expression for MMP-2 when cultured on the synthetic topographically patterned membrane. For both cell types, the synthetic topographically patterned membrane had no significant effect on the expression of PECAM, indicating the endothelial cell type was unaltered by the topographic cues.

DISCUSSION

A number of aspects associated with these highly porous substrates make them ideal candidates for studying the relationship between cellular behavior and topographic cues. First and foremost is the similarity of the synthetic membrane to the basement membrane of in vivo tissues. These substrates intrinsically possess a number of the common topographic features of basement membranes with stochastic surface order. They are easy to fabricate, with the porosity of the substrate easily modified by slight changes in the pH of the dipping solution. A recent work (24) has used this property to study the effect of pore size on corneal epithelial cell behavior when adhered to a final PAA layer of the porous PEM (both corneal basement membrane and Descemet's membrane have topographic

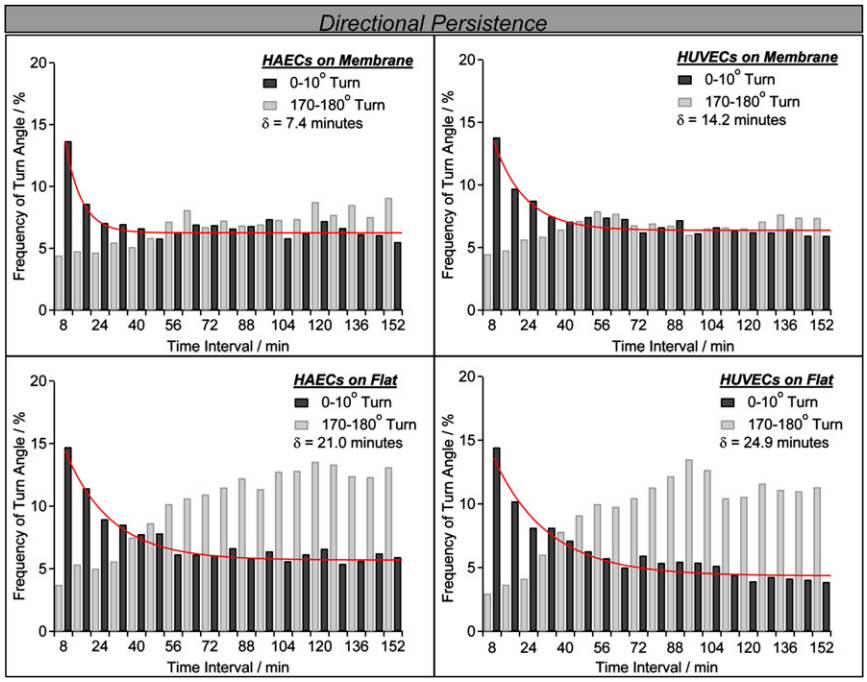

FIGURE 4 Directional persistence of HUVECs and HAECs as a function of substrate type (visually noted when the frequency of persistent motion became approximately constant with the increasing observation time interval; additionally quantified by the decay length of the exponential fit, δ). The frequency of turning angles is expressed as a percentage of the total. When cultured on the synthetic membrane, both HUVECs and HAECs had a decreased directional persistence time (~30 min) and decay length when compared to the persistence time (~60 min) and decay length on flat surfaces. When cultured on flat surfaces, both HUVECs and HAECs also had an increased preponderance for returning along their forward migration path, as noted by the increasing percentage of antipersistent turns over persistent turns, after the 60 min directional persistence time interval.

features that are similar to vascular basement membrane (25)). In contrast to the published corneal work, we have employed soft lithography to fabricate a large number of these surfaces with identical topographies. This process helps to decrease the systematic error associated with reproducibility of the porous features on separate surfaces. Soft lithography also allows for replicates of the PEM topography to be generated on any piece of cell cultureware, as well as for the potential to transfer the topography onto implantable bioengineered surfaces. However, if the chemistry of the PEM is experimentally required, we have found that amine termination of the glass slide with APS will ensure that the porous PEM remains bound to the glass during long-term cell culture conditions. By using a small number of PEM layers, these porous substrates were also sufficiently transparent and could be used in a number of light microscopy-related cell and molecular biology experiments. Finally, as mentioned previously, the topographic features associated with vascular basement membranes are conserved in a number of other in vivo basement membranes (25). This makes these synthetic topographic substrates highly relevant for diverse fields of investigation.

In aggregate, these topographically biomimetic surfaces had a significant impact on a number of cell behaviors, including cell migration and proliferation, which are involved in the maintenance of homeostasis in vascular tissues. During the normal life span of the vasculature and following surgical intervention in cardiovascular disease, vascular endothelial cells are important in the repopulation of denuded endothelium and their primary mechanism is to do this through proliferation and migration. Dysregulation of the substratum is known to occur during cardiovascular disease onset and progression and these changes are correlated with dysregulation of vascular endothelial cells. The motility of both HUVECs and HAECs was significantly altered by the presentation of the biomimetic topographies, both in terms of the velocity at which the cells migrate, but also in terms of the cells' ability to maintain their directional persistence during migration. Migration and directional persistence are important factors in such biological processes as embryogenesis (26), immune response (27), and wound healing (28). In the absence of externally directed cell migration, e.g., durotaxis (29) or chemotaxis (30), both the HUVECs and HAECs in this study were observed to have an intrinsic directional persistence time that was influenced by the stochastic topography of the underlying surface. Changes in directional persistence time, associated with the static stiffness (not durotaxis) of the topography, may shed light on the important role that stochastic topographies play on the residence time of cells in tissues whose mechanics have been altered by disease, therapeutic intervention, or by the wound healing process. Topographically patterned anisotropic ridges and grooves in the biomimetic range (31), have been shown to guide both HUVEC and HAEC migration along the path of the ridge, and in the case of HUVECs, significantly decreased both the migration and proliferation rate. In the present case, these endothelial cells are interacting with an assortment of ridges, pores, and bumps that are randomly presented to the adhered cell. Consequently, the cells are not contact guided (12) by long-range order of the substratum and therefore have a decreased directional

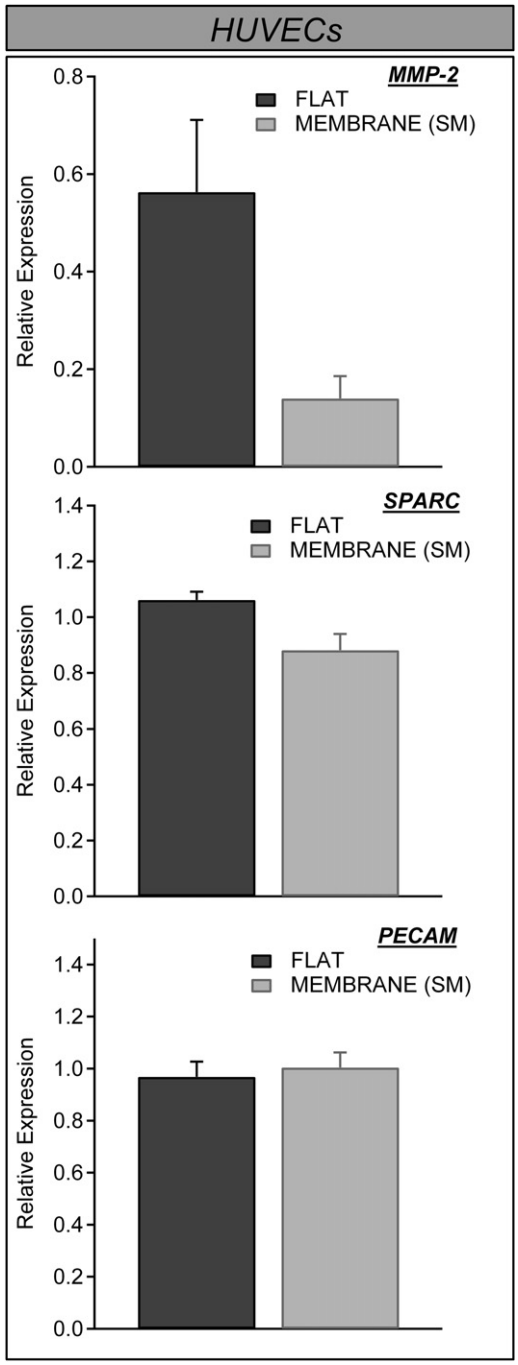

FIGURE 5 Gene expression of MMP-2, SPARC, and PECAM from HUVECs cultured on flat or synthetic membrane surfaces. Both MMP-2 and SPARC trended toward decreased expression when cultured on the topographic membrane, however only MMP-2 was significant ($p < 0.001$). PECAM was unaffected by the topography.

persistence time. In contrast to the ridge and groove topographies, migration rates were increased on these substrates for both cell types.

On the biomimetic topographic features, both HUVECs and HAECs were shown here to have a decreased proliferation rate as compared to flat surfaces. A link between nuclear volume and proliferation rate has recently been suggested for cells on ridge and groove topographies (5) as well as for micropatterned circles and squares of fibronectin (32). Although not studied here, future work could focus on cytoskeletal and nuclear shape changes associated with cells on these synthetic membranes to determine if they impact the proliferation rate of the HUVECs and HAECs.

In vivo regulation (SPARC) (33) and remodeling (MMPs) (34) of extracellular matrix occur in a number of important biological processes, including angiogenesis (35), wound healing (36), invasion (37), and inflammation (38). MMP-2 was significantly decreased by the presentation of the synthetic membrane in HUVECs, indicating a decreased remodeling response to the surface that best reflected the in vivo topographic environment of the cell. Although the trends were similar for expression of MMP-2 in HAECs, it was not significantly altered by the presentation of the topography alone. Similar to other reports of endothelial cells on substratum topography (39), these synthetic membranes did not change PECAM expression, although TNF-α has been shown to downregulate the expression of PECAM (40). To our knowledge, there are no previous investigations into the expression of PECAM in HAECs on a biologically relevant topography in the presence of inflammatory cytokines. All of the genes were significantly decreased (as compared to flats) when cells were exposed to elevated levels of TNF-α, a known factor associated with end-stage heart failure (41). MMP-2 expression has been shown to be increased and participates in the matrix remodeling that occurs during atherosclerotic lesion formation (42). The dramatic downregulation of MMP-2 in TNF-α treated HAECs on the topographically patterned membrane suggests the in vivo topography may be associated with both the onset and progression of cardiovascular disease. SPARC has been shown to be important in collagen deposition and remodeling in multiple forms of cardiovascular disease (43). The downregulation of SPARC in TNF-α stimulated HAECs on the synthetic membrane demonstrates that a biologically relevant topography may be important in modulating the inflammatory response of arterial endothelial cells. The expression of ICAM-1 on the synthetic membrane was also significantly decreased for HAECs, when the cells were induced to express ICAM-1 by exposure to TNF-α (44). In aggregate, these results suggest that the inflammatory response of HAECs may be altered by substratum topographic cues alone and indicates the potential to decrease inflammation by controlling matrix remodeling and the potential for reducing adhesion and invasion of leukocytes on a full endothelial cell layer (45). Bioengineered implants with similar topographies may therefore have a decreased probability of rejection. A building body of knowledge emerging from our lab and others suggests that the presence of biomimetic cues participates

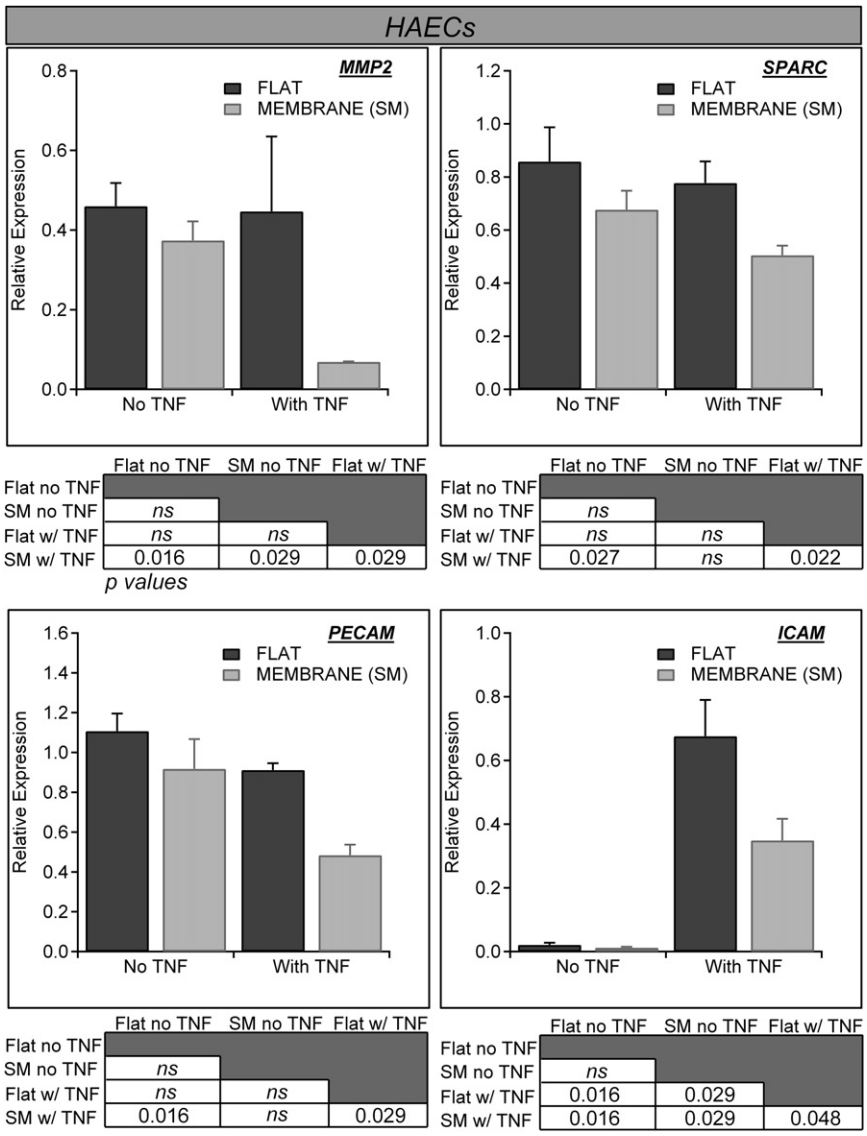

FIGURE 6 Gene expression for MMP-2, SPARC, PECAM, and ICAM-1, both in the presence and absence of 10 ng/ml TNF-α, as a function of substrate topography. Significance values for various comparisons are located in the boxes below the bar graphs. Although the trend for gene expression of MMP-2 and SPARC were similar to HUVECs, the topography alone did not significantly downregulate the expression. With the exception of ICAM-1, there was no significant difference in the gene expression of MMP-2, SPARC, or PECAM when cells cultured on the flat surfaces were exposed to TNF-α, there were, however, significant decreases in gene expression for cells on the synthetic membrane.

in stabilizing cellular phenotype, contributing to the maintenance of homeostasis.

CONCLUSION

This study has shown that a number of important endothelial cell behaviors can be modified by the presentation of a stochastic topographic cue that closely mimics the topographic environment of many vascular basement membranes found in the body. The ease of fabrication and the ability to replicate the porosity of the PEM using soft lithography makes these substrates an ideal construct to investigate topographic cueing on cellular behavior. In addition to changes in basic cell motility and proliferation, the presentation of the synthetic membrane significantly altered the expression of a number of important genes that regulate tissue remodeling and inflammatory response. The significant decrease in expression of several cardiovascular disease-related genes, in response to TNF-α on these substrates, suggests incorporation of the topographies onto bioengineered surfaces may facilitate, in conjunction with traditional therapies, long-term acceptance of vascular implants.

SUPPORTING MATERIAL

A detailed description of the cell tracker algorithm, two figures, and a movie are available at http://www.biophysj.org/biophysj/supplemental/S0006-3495(12)00170-1.

The authors acknowledge technical discussion with Dr. Nihar Shah.

This work was supported by the National Institutes of Health (R01EY01613404, 1R01HL079012-01A1 and P30EY12576) and an unrestricted grant from Research to Prevent Blindness.

REFERENCES

1. Discher, D. E., P. Janmey, and Y. L. Wang. 2005. Tissue cells feel and respond to the stiffness of their substrate. *Science.* 310:1139–1143.
2. Dalby, M. J. 2007. Cellular response to low adhesion nanotopographies. *Int. J. Nanomedicine.* 2:373–381.
3. Gasiorowski, J. Z., S. J. Liliensiek, …, C. J. Murphy. 2010. Alterations in gene expression of human vascular endothelial cells associated with nanotopographic cues. *Biomaterials.* 31:8882–8888.
4. McKee, C. T., J. A. Wood, …, P. Russell. 2011. The effect of biophysical attributes of the ocular trabecular meshwork associated with glaucoma on the cell response to therapeutic agents. *Biomaterials.* 32:2417–2423.
5. McKee, C. T., V. K. Raghunathan, …, C. J. Murphy. 2011. Topographic modulation of the orientation and shape of cell nuclei and their influence on the measured elastic modulus of epithelial cells. *Biophys. J.* 101:2139–2146.
6. Chen, C. S., M. Mrksich, …, D. E. Ingber. 1998. Micropatterned surfaces for control of cell shape, position, and function. *Biotechnol. Prog.* 14:356–363.
7. Truscott, R. J. 2009. Presbyopia. Emerging from a blur towards an understanding of the molecular basis for this most common eye condition. *Exp. Eye Res.* 88:241–247.
8. Last, J. A., T. Pan, …, P. Russell. 2011. Elastic modulus determination of normal and glaucomatous human trabecular meshwork. *Invest. Ophthalmol. Vis. Sci.* 52:2147–2152.
9. Kymionis, G. D., D. M. Portaliou, …, S. H. Yoo. 2007. Herpetic keratitis with iritis after corneal cross-linking with riboflavin and ultraviolet A for keratoconus. *J. Cataract Refract. Surg.* 33:1982–1984.
10. Dickinson, R. B., S. Guido, and R. T. Tranquillo. 1994. Biased cell migration of fibroblasts exhibiting contact guidance in oriented collagen gels. *Ann. Biomed. Eng.* 22:342–356.
11. Kleinman, H. K., and G. R. Martin. 2005. Matrigel: basement membrane matrix with biological activity. *Semin. Cancer Biol.* 15:378–386.
12. Teixeira, A. I., G. A. Abrams, …, P. F. Nealey. 2003. Epithelial contact guidance on well-defined micro- and nanostructured substrates. *J. Cell Sci.* 116:1881–1892.
13. Odom, T. W., C. Love, …, G. M. Whitesides. 2002. Improved pattern transfer in soft lithography using composite stamps. *Langmuir.* 18:5314–5320.
14. Xia, Y., and G. M. Whitesides. 1998. Soft lithography. *Annu. Rev. Mater. Sci.* 28:153–184.
15. Ghassemi, S., N. Biais, …, J. Hone. 2008. Fabrication of elastomer pillar arrays with modulated stiffness for cellular force measurements. *J. Vac. Sci. Technol. B Microelectron. Nanometer Struct. Process Meas. Phenom.* 26:2549–2553.
16. Karuri, N. W., T. J. Porri, …, P. F. Nealey. 2006. Nano- and microscale holes modulate cell-substrate adhesion, cytoskeletal organization, and -beta1 integrin localization in SV40 human corneal epithelial cells. *IEEE Trans. Nanobioscience.* 5:273–280.
17. Liliensiek, S. J., P. Nealey, and C. J. Murphy. 2009. Characterization of endothelial basement membrane nanotopography in rhesus macaque as a guide for vessel tissue engineering. *Tissue Eng. Part A.* 15:2643–2651.
18. Hironaka, K., H. Makino, …, Z. Ota. 1993. Renal basement membranes by ultrahigh resolution scanning electron microscopy. *Kidney Int.* 43:334–345.
19. Inoue, S. 1994. Basic structure of basement membranes is a fine network of "cords," irregular anastomosing strands. *Microsc. Res. Tech.* 28:29–47.
20. Abrams, G. A., C. J. Murphy, …, D. E. Bjorling. 2003. Ultrastructural basement membrane topography of the bladder epithelium. *Urol. Res.* 31:341–346.
21. Mendelsohn, J. D., C. J. Barret, …, M. F. Rubner. 2000. Fabrication of microporous thin films from polyelectrolyte multilayers. *Langmuir.* 16:5017–5023.
22. Decher, G., J. D. Hong, and J. Schmitt. 1992. Buildup of ultrathin multilayer films by a self-assembly process. 3. Consecutively alternating adsorption of anionic and cationic polyelectrolytes on charged surfaces. *Thin Solid Films.* 210:831–835.
23. Petrie, R. J., A. D. Doyle, and K. M. Yamada. 2009. Random versus directionally persistent cell migration. *Nat. Rev. Mol. Cell Biol.* 10:538–549.
24. Hajicharalambous, C. S., J. Lichter, …, P. Rajagopalan. 2009. Nano- and sub-micron porous polyelectrolyte multilayer assemblies: biomimetic surfaces for human corneal epithelial cells. *Biomaterials.* 30:4029–4036.
25. Abrams, G. A., S. S. Schaus, …, C. J. Murphy. 2000. Nanoscale topography of the corneal epithelial basement membrane and Descemet's membrane of the human. *Cornea.* 19:57–64.
26. Thiery, J. P., J. L. Duband, and G. C. Tucker. 1985. Cell migration in the vertebrate embryo: role of cell adhesion and tissue environment in pattern formation. *Annu. Rev. Cell Biol.* 1:91–113.
27. Sallusto, F., and A. Lanzavecchia. 2000. Understanding dendritic cell and T-lymphocyte traffic through the analysis of chemokine receptor expression. *Immunol. Rev.* 177:134–140.
28. Zhao, M. 2009. Electrical fields in wound healing-an overriding signal that directs cell migration. *Semin. Cell Dev. Biol.* 20:674–682.
29. Lo, C. M., H. B. Wang, …, Y. L. Wang. 2000. Cell movement is guided by the rigidity of the substrate. *Biophys. J.* 79:144–152.
30. Chen, L., M. Iijima, …, P. N. Devreotes. 2007. PLA2 and PI3K/PTEN pathways act in parallel to mediate chemotaxis. *Dev. Cell.* 12:603–614.
31. Liliensiek, S. J., J. A. Wood, …, C. J. Murphy. 2010. Modulation of human vascular endothelial cell behaviors by nanotopographic cues. *Biomaterials.* 31:5418–5426.
32. Roca-Cusachs, P., J. Alcaraz, …, D. Navajas. 2008. Micropatterning of single endothelial cell shape reveals a tight coupling between nuclear volume in G1 and proliferation. *Biophys. J.* 94:4984–4995.
33. Chlenski, A., and S. L. Cohn. 2010. Modulation of matrix remodeling by SPARC in neoplastic progression. *Semin. Cell Dev. Biol.* 21:55–65.
34. Li, Y. Y., C. F. McTiernan, and A. M. Feldman. 2000. Interplay of matrix metalloproteinases, tissue inhibitors of metalloproteinases and their regulators in cardiac matrix remodeling. *Cardiovasc. Res.* 46:214–224.
35. Yunker, C. K., W. Golembieski, …, S. A. Rempel. 2008. SPARC-induced increase in glioma matrix and decrease in vascularity are associated with reduced VEGF expression and secretion. *Int. J. Cancer.* 122:2735–2743.
36. Lemaître, V., and J. D'Armiento. 2006. Matrix metalloproteinases in development and disease. *Birth Defects Res. C Embryo Today.* 78:1–10.
37. Kim, Y. M., J. W. Jang, …, Y. G. Kwon. 2000. Endostatin inhibits endothelial and tumor cellular invasion by blocking the activation and catalytic activity of matrix metalloproteinase. *Cancer Res.* 60:5410–5413.
38. Kelly, K. A., J. R. Allport, …, R. Weissleder. 2007. SPARC is a VCAM-1 counter-ligand that mediates leukocyte transmigration. *J. Leukoc. Biol.* 81:748–756.
39. Bettinger, C. J., Z. Zhang, …, R. Langer. 2008. Enhancement of in vitro capillary tube formation by substrate nanotopography. *Adv. Mater.* 20:99–103.
40. Stewart, R. J., T. S. Kashour, and P. A. Marsden. 1996. Vascular endothelial platelet endothelial adhesion molecule-1 (PECAM-1) expression is decreased by TNF-alpha and IFN-gamma. Evidence for cytokine-induced destabilization of messenger ribonucleic acid transcripts in bovine endothelial cells. *J. Immunol.* 156:1221–1228.
41. Levine, B., J. Kalman, …, M. Packer. 1990. Elevated circulating levels of tumor necrosis factor in severe chronic heart failure. *N. Engl. J. Med.* 323:236–241.

42. Li, Z., L. Li, …, E. G. Lakatta. 1996. Increased expression of 72-kd type IV collagenase (MMP-2) in human aortic atherosclerotic lesions. *Am. J. Pathol.* 148:121–128.

43. McCurdy, S., C. F. Baicu, …, A. D. Bradshaw. 2010. Cardiac extracellular matrix remodeling: fibrillar collagens and Secreted Protein Acidic and Rich in Cysteine (SPARC). *J. Mol. Cell. Cardiol.* 48:544–549.

44. Burke-Gaffney, A., and P. G. Hellewell. 1996. Tumour necrosis factor-alpha-induced ICAM-1 expression in human vascular endothelial and lung epithelial cells: modulation by tyrosine kinase inhibitors. *Br. J. Pharmacol.* 119:1149–1158.

45. van Griensven, M., C. Probst, …, H. C. Pape. 2006. Leukocyte-endothelial interactions via ICAM-1 are detrimental in polymicrobial sepsis. *Shock.* 25:254–259.